

A Numerical Study of Raindrop Impact Phenomena: The Elastic Deformation Case¹

C. HUANG, J. M. BRADFORD, AND J. H. CUSHMAN²

ABSTRACT

Understanding the deformation processes of soil material under raindrop impact is a basic step in studying soil resistance against particle detachment by raindrop splash. To simulate the deformation pattern of a solid material under impact, we used the finite difference technique to solve the dynamic equation of linear elasticity. The selected material properties resembled soil media of wide ranges of elasticity. Two types of impact loading were imposed: a steady, uniform load and a simulated raindrop impact load. Materials responded differently under these loading conditions and showed dissimilar deformation patterns. For a material with low modulus of elasticity, a uniform depression was found under steady, uniform load, while a cone-shaped depression was shown under simulated raindrop impact. The shape of the surface deformation gave us insight into the mechanism of material detachment. The interaction of the lateral jet stream and the obstacles in its course are believed to be the major factor in determining the material detachment. The obstacles can be the sides of the cavity or the irregularities on the granular material itself.

Additional Index Words: soil erosion, finite difference method.

Huang, C., J.M. Bradford, and J.H. Cushman. 1983. A numerical study of raindrop impact phenomena: the elastic deformation case. *Soil Sci. Soc. Am. J.* 47:855-861.

UNDERSTANDING THE DEFORMATION PROCESSES of soil material under raindrop impact is the basic step in studying the mechanics of soil resistance against splash detachment. If we examine the processes involved in the impact-detachment phenomena, two major modes of action can be identified. They are the surface compression from the impulsive load and the lateral jetting streams that carry the eroded particles. The manner in which the soil surface deforms under the raindrop impact determines the angle of incidence between the jet stream and the soil material and, subsequently, the amount of the detachment. Thus, it is imperative to study the transient deformation of the soil surface in order to better describe the impact phenomena.

Raindrop impact erosion has been the subject of broad interest in the fields of material engineering (Fyall and King, 1970, 1974). Engineers have dealt with problems of material erosion, for example, the erosion of airplane wings, windows, and helicopter blades while flying through rainstorms, and the erosion of steam turbine blades. Although the subject materials and the impact environment that the engineers have been confronted with are quite different from the natural raindrop-soil splash erosion, the basic principles are readily deductible. Experimental techniques, such as high-speed photography and transducer monitoring, have provided valuable information in de-

scribing the flow regime as well as in registering the impact force. The lack of a microscopic delineation with these techniques prevents us from compiling a complete mechanistic model of the impact process.

Geotechnical engineers study the deformation of soil materials, but most of their works deal with the rigid loads, either statically or dynamically. The classical Boussinesq solution represents the stress distribution in the soil domain at equilibrium (p. 158, Winterkorn and Fang, 1975). Raindrop impact-soil deformation has the characteristic of transient, nonrigid loading in which the soil surface deforms without the confinement of the projectile surfaces. The nonuniform, unsteady nature of the raindrop impact deviates greatly from the stress conditions normally analyzed by most civil engineers.

In this study, we will numerically examine the deformation pattern of a soil medium at the initial stage of raindrop impact. The dynamic equations of linear elasticity will be solved for materials in which the mechanical properties resemble soil media of wide ranges of elasticity. Numerical results will be used to demonstrate the time history of the deformed surface of an elastic medium with different compressional properties.

THE BASIC DYNAMIC EQUATIONS

The equation of motion in a homogeneous isotropic elastic medium is given by

$$(\lambda + 2G)\nabla(\nabla \cdot D) - G\nabla \times \nabla \times D - \rho \partial^2 D / \partial t^2 = 0, \quad [1]$$

where D is the displacement vector, ρ is the density of the solid material, t is time, λ and G are the Lamé's constants, ∇ is the gradient operator, $\nabla \cdot$ is the divergence operator, and $\nabla \times$ is the curl operator (Richart et al., 1970). Note that G is also called the shear modulus or the rigidity modulus. Expressing Eq. [1] in a cylindrical coordinate system, and assuming axisymmetric conditions, we can rewrite Eq. [1] as

$$(\lambda + 2G) \left(\frac{\partial^2 D_r}{\partial r^2} + \frac{1}{r} \frac{\partial D_r}{\partial r} - \frac{D_r}{r^2} + \frac{\partial^2 D_z}{\partial r \partial z} \right) - G \left(\frac{\partial^2 D_z}{\partial r \partial z} - \frac{\partial^2 D_r}{\partial z^2} \right) = \rho \frac{\partial^2 D_r}{\partial t^2}, \quad [2]$$

and

$$(\lambda + 2G) \left(\frac{\partial^2 D_z}{\partial z^2} + \frac{1}{r} \frac{\partial D_r}{\partial z} + \frac{\partial^2 D_r}{\partial r \partial z} \right) - G \left(\frac{\partial^2 D_r}{\partial r \partial z} - \frac{\partial^2 D_z}{\partial r^2} + \frac{1}{r} \frac{\partial D_r}{\partial z} - \frac{1}{r} \frac{\partial D_z}{\partial r} \right) = \rho \frac{\partial^2 D_z}{\partial t^2}, \quad [3]$$

where D_r and D_z are radial (r) and axial (z) components of the displacement vector D . The assumption of axisymmetry implies that the circumferential or angular displacement, D_θ , is zero and D_r and D_z are invariant in θ , this simplifies the

¹ Contribution from the USDA-ARS in cooperation with the Agronomy Dep., Purdue Univ. Journal no. 9145. Received 31 Aug. 1982. Approved 16 May 1983.

² Former Graduate Assistant, Soil Scientist, USDA-ARS, and Associate Professor, Dep. of Agronomy, Purdue Univ., West Lafayette, IN 47907. The Senior Author is now Research Associate, Dep. of Hydrology and Water Resources, Univ. of Arizona, AZ 85721.

problem from three dimensional to a two-dimensional one. The interrelationships among Lamé's constants, λ and G , and other solid properties, such as Young's modulus, E , and the Poisson's ratio, ν , are given below:

$$\begin{aligned} G &= 0.5E/(1+\nu), \\ \lambda &= E\nu/(1-2\nu)(1+\nu), \\ \nu &= 0.5\lambda/(\lambda+G), \\ E &= G(3\lambda+2G)/(\lambda+G). \end{aligned} \quad [4]$$

The stress wave propagation velocities in an elastic medium are defined as

$$V_c = [(\lambda + 2G)/\rho]^{1/2}, \quad [5]$$

and

$$V_s = (G/\rho)^{1/2}, \quad [6]$$

where V_c in the compressional wave velocity and V_s is the shear wave velocity (p. 77-78, Richart et al., 1970).

The displacement-strain-stress relationships (or Hooke's law) for elastic materials are given below:
Strain components:

$$\begin{aligned} \epsilon_r &= \frac{\partial D_r}{\partial r}, & \epsilon_z &= \frac{\partial D_z}{\partial z}, & \epsilon_\theta &= \frac{D_r}{r}, \\ \gamma_{rz} &= \gamma_{zr} = \frac{\partial D_r}{\partial z} + \frac{\partial D_z}{\partial r}; \end{aligned} \quad [7]$$

Stress components:

$$\begin{aligned} \sigma_r &= (\lambda + 2G) (\epsilon_r + \epsilon_z + \epsilon_\theta) - 2G (\epsilon_z + \epsilon_\theta), \\ \sigma_z &= (\lambda + 2G) (\epsilon_r + \epsilon_z + \epsilon_\theta) - 2G (\epsilon_r + \epsilon_\theta), \\ \sigma_\theta &= (\lambda + 2G) (\epsilon_r + \epsilon_z + \epsilon_\theta) - 2G (\epsilon_r + \epsilon_z), \\ \tau_{rz} &= \tau_{zr} = G\gamma_{rz} \end{aligned} \quad [8]$$

where $\epsilon_r, \epsilon_z, \epsilon_\theta$ are the normal strains, γ_{rz} and γ_{zr} are the shear strains, $\sigma_r, \sigma_z, \sigma_\theta$ are the normal stresses, and the τ_{rz} and τ_{zr} are the shear stresses. The axisymmetry condition does not imply that the circumferential (or angular) stress and strain, σ_θ and ϵ_θ , vanish.

The elastic half-space is originally at rest. Thus, we have the following initial conditions:

$$D_{r(r,z,0)} = D_{z(r,z,0)} = 0. \quad [9]$$

The boundary conditions along the axis of symmetry ($r = 0$) are

$$D_{r(0,z,t)} = 0, \quad [10]$$

and

$$\partial D_{z(0,z,t)} / \partial r = 0. \quad [11]$$

The surface boundary conditions ($z = 0$) are:

$$\sigma_{z(r,0,t)} = F(r,t), \quad [12]$$

and

$$\tau_{rz(r,0,t)} = 0, \quad [13]$$

where $F(r,t)$ is the surface loading function. A center-time-center-space finite difference scheme is formulated to solve the basic dynamics equations. The results show the response of an elastic half space under dynamic loading conditions, which simulates the soil surface deformation from a rain-drop impact.

THE NUMERICAL SCHEMES

The domain of calculation is given in Fig. 1. The equations of motion (Eq. [2] and Eq. [3]) are written in finite difference form by replacing the various de-

rivates by their centered difference approximations (Alterman and Karal, 1968). If we let $r = \ell \cdot \Delta r$ and $z = m \cdot \Delta z$, where Δr and Δz are incremental lengths along the r and z axes, and let $t = n \cdot \Delta t$, where Δt is an increment in time, and use subscripts (ℓ, m) and superscript n to represent space-time domain (r, z, t), Eq. [2] becomes

$$\begin{aligned} (\lambda + 2G) &\left\{ \frac{1}{\Delta r^2} [D_{r(\ell+1,m)}^n - 2D_{r(\ell,m)}^n + D_{r(\ell-1,m)}^n] \right. \\ &+ \frac{1}{2l\Delta r^2} [D_{r(\ell+1,m)}^n - D_{r(\ell-1,m)}^n] - \frac{1}{l^2\Delta r^2} D_{r(\ell,m)}^n \\ &+ \frac{1}{4\Delta r\Delta z} \times [D_{z(\ell+1,m+1)}^n - D_{z(\ell+1,m-1)}^n \\ &- D_{z(\ell-1,m+1)}^n + D_{z(\ell-1,m-1)}^n] \left. \right\} \\ &- G \left\{ \frac{1}{4\Delta r\Delta z} [D_{z(\ell+1,m+1)}^n - D_{z(\ell+1,m-1)}^n \right. \\ &- D_{z(\ell-1,m+1)}^n + D_{z(\ell-1,m-1)}^n] \\ &+ \frac{1}{\Delta z^2} [D_{r(\ell,m+1)}^n - 2D_{r(\ell,m)}^n + D_{r(\ell,m-1)}^n] \left. \right\} \\ &= \rho \frac{1}{\Delta t^2} [D_{r(\ell,m)}^{n+1} - 2D_{r(\ell,m)}^n + D_{r(\ell,m)}^{n-1}]. \quad [14] \end{aligned}$$

Rearranging terms, and using the definition of wave velocities in the elastic medium, Eq. [14] may be written

$$D_{r(\ell,m)}^{n+1} = 2D_{r(\ell,m)}^n - D_{r(\ell,m)}^{n-1} + \left(\frac{V_c\Delta t}{\Delta r} \right)^2$$

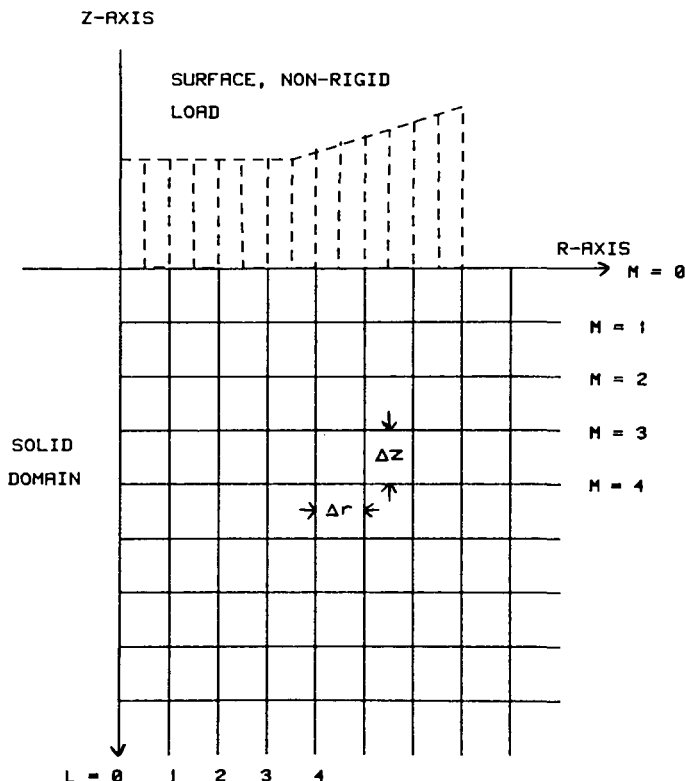


Fig. 1—The solid calculation domain and its discretization.

$$\begin{aligned} & \times \left\{ \left[D_{r(l+1,m)}^n - 2D_{r(l,m)}^n + D_{r(l-1,m)}^n \right] \right. \\ & + \frac{1}{2l} \left[D_{r(l+1,m)}^n - D_{r(l-1,m)}^n \right] - \frac{1}{l^2} D_{r(l,m)}^n \\ & + \frac{\Delta r}{4\Delta z} \left[1 - \left(\frac{V_S}{V_C} \right)^2 \right] \\ & \times \left[D_{z(l+1,m+1)}^n - D_{z(l+1,m-1)}^n \right. \\ & - D_{z(l-1,m+1)}^n + D_{z(l-1,m-1)}^n \left. \right] + \left(\frac{\Delta r}{\Delta z} \right)^2 \left(\frac{V_S}{V_C} \right)^2 \\ & \times \left. \left[D_{r(l,m+1)}^n - 2D_{r(l,m)}^n + D_{r(l,m-1)}^n \right] \right\}. \quad [15] \end{aligned}$$

Likewise, Eq. [3] can also be written as

$$\begin{aligned} D_{z(l,m)}^{n+1} &= 2D_{z(l,m)}^n - D_{r(l,m)}^{n-1} + \left(\frac{V_C \Delta t}{\Delta r} \right)^2 \\ & \times \left\{ \left(\frac{\Delta r}{\Delta z} \right)^2 \left[D_{z(l,m+1)}^n - 2D_{z(l,m)}^n + D_{z(l,m-1)}^n \right] \right. \\ & + \frac{\Delta r}{2l\Delta z} \left[1 - \left(\frac{V_S}{V_C} \right)^2 \right] \\ & \times \left[D_{r(l,m+1)}^n - D_{r(l,m-1)}^n \right] + \frac{\Delta r}{4\Delta z} \left[1 - \left(\frac{V_S}{V_C} \right)^2 \right] \\ & \times \left[D_{r(l+1,m+1)}^n - D_{r(l+1,m-1)}^n \right. \\ & - D_{r(l-1,m+1)}^n + D_{r(l-1,m-1)}^n \left. \right] \\ & + \frac{1}{2l} \left(\frac{V_S}{V_C} \right)^2 \left[D_{r(l+1,m)}^n - D_{r(l-1,m)}^n \right] \\ & + \left. \left(\frac{V_S}{V_C} \right)^2 \left[D_{z(l,m+1)}^n - 2D_{z(l,m)}^n + D_{z(l,m-1)}^n \right] \right\}. \quad [16] \end{aligned}$$

Equations [15] and [16] are suitable for the interior of the solid domain. Along the axis of symmetry ($l = 0$), Eq. [15] and Eq. [16] are undefined because of the presence of l in the denominator. From the symmetric boundary conditions that we have imposed, the radial displacement is zero along the axis of symmetry, hence,

$$D_{r(0,m)}^n = 0. \quad [17]$$

To evaluate axial displacement along the axis of symmetry is more complicated. The undefined terms in Eq. [3] are $\partial D_r / r \partial z$ and $\partial D_z / r \partial r$. By using L'Hospital's rule, these terms can be approximated as:

$$\frac{1}{r} \frac{\partial D_r}{\partial z} \approx \frac{\partial^2 D_r}{\partial r \partial z}, \quad \frac{1}{r} \frac{\partial D_z}{\partial r} \approx \frac{\partial^2 D_z}{\partial r^2}. \quad [18]$$

From axisymmetry conditions, we have

$$D_{r(-1,m)}^n = -D_{r(1,m)}^n,$$

and

$$D_{z(-1,m)}^n = D_{z(1,m)}^n. \quad [19]$$

Expression [19] can be approximated by the following:

$$\begin{aligned} \frac{\partial^2 D_z}{\partial r^2} \Big|_{r=0} &\approx \frac{D_{z(1,m)}^n - 2D_{z(0,m)}^n + D_{z(-1,m)}^n}{\Delta r^2} \\ &\approx \frac{2 \left[D_{z(1,m)}^n - D_{z(0,m)}^n \right]}{\Delta r^2}, \quad [20] \end{aligned}$$

and

$$\begin{aligned} \frac{\partial^2 D_r}{\partial r \partial z} \Big|_{r=0} &\approx \frac{D_{r(1,m+1)}^n - D_{r(-1,m+1)}^n - D_{r(-1,m-1)}^n + D_{r(1,m-1)}^n}{4\Delta r \Delta z} \\ &\approx \frac{D_{r(1,m+1)}^n - D_{r(1,m-1)}^n}{2\Delta r \Delta z}. \quad [21] \end{aligned}$$

Thus, the finite difference form of Eq. [3] for axial displacement along the axis of symmetry can be expressed as

$$\begin{aligned} D_{z(0,m)}^{n+1} &= 2D_{z(0,m)}^n - D_{r(0,m)}^{n-1} + \left(\frac{V_C \Delta t}{\Delta r} \right)^2 \\ & \times \left\{ \left[D_{z(0,m+1)}^n - 2D_{z(0,m)}^n + D_{z(0,m-1)}^n \right] \right. \\ & + \frac{\Delta r}{\Delta z} \left[1 - \left(\frac{V_S}{V_C} \right)^2 \right] \left[D_{r(1,m+1)}^n - D_{r(1,m-1)}^n \right] \\ & + \left. 4 \left(\frac{V_S}{V_C} \right)^2 \left[D_{z(1,m)}^n - D_{z(0,m)}^n \right] \right\}. \quad [22] \end{aligned}$$

The finite difference Eq. [15], [16], and [22] cannot be applied at the free surface ($z=0$), because these equations involve undefined quantities, $D_{r(l,-1)}^n$ and $D_{z(l,-1)}^n$. In order to calculate the displacements in this special case, we need to use the surface boundary conditions. Combining the surface boundary conditions and the basic stress-strain-displacement relationship, we have

$$\begin{aligned} \sigma_z &= (\lambda + 2G) \left(\frac{\partial D_r}{\partial r} + \frac{D_r}{r} + \frac{\partial D_z}{\partial z} \right) - 2G \left(\frac{\partial D_r}{\partial r} + \frac{D_r}{r} \right) \\ &= F(r, t), \quad [23] \end{aligned}$$

and

$$\tau_{rz} = G \left(\frac{\partial D_r}{\partial z} + \frac{\partial D_z}{\partial r} \right) = 0. \quad [24]$$

Writing out in finite difference form and rearranging terms, we have

$$\begin{aligned} D_{z(l,-1)}^n &= D_{z(l,1)}^n + 2\Delta z V_C^2 F_{(l)}^n + \frac{\Delta z}{\Delta r} \left[1 - \left(\frac{V_S}{V_C} \right)^2 \right] \\ & \times \left[D_{r(l+1,0)}^n - D_{r(l-1,0)}^n - \frac{2}{l} D_{r(l,0)}^n \right], \quad [25] \end{aligned}$$

and

$$D_{r(l,-1)}^n = D_{r(l,1)}^n + \frac{\Delta z}{\Delta r} \left[D_{z(l+1,0)}^n - D_{z(l-1,0)}^n \right]. \quad [26]$$

A special situation in the surface boundary is when $r = 0$ and $z = 0$. Symmetry boundary conditions imply that $D_{r(0,-1)}^n = 0$. Using L'Hospital's rule, D_r/r can be approximated by $\partial D_r / \partial r$ and Eq. [25] is written as

$$\begin{aligned}
 D_{z(0,-1)}^n &= D_{z(0,1)}^n + 2\Delta z V_c^2 F_{(1)}^n \\
 &+ 2\left(\frac{\Delta z}{\Delta r}\right)\left[1 - \left(\frac{V_s}{V_c}\right)^2\right]\left[D_{r(1,0)}^n - D_{r(-1,0)}^n\right] \\
 &= D_{z(0,1)}^n + 2\Delta z V_c^2 F_{(1)}^n \\
 &+ 4\left(\frac{\Delta z}{\Delta r}\right)\left[1 - \left(\frac{V_s}{V_c}\right)^2\right]D_{r(1,0)}^n \quad [27]
 \end{aligned}$$

The stability constraint of the scheme is

$$\frac{\Delta t}{\Delta r} < \frac{1}{(V_c^2 + V_s^2)^{1/2}} \quad [28]$$

where V_c and V_s are the compressional and shear velocities, respectively (Alterman and Karal, 1968).

All the finite difference equations are explicit in nature, thus the solution procedure is straight forward. The steps of the numerical procedures are as follows:

1. Evaluate the displacement at the surface boundary using Eq. [25], [26], and [27].
2. Use Eq. [22] to calculate the axial displacement along the axis of symmetry.
3. Use Eq. [15] and [16] to calculate the axial and radial displacements within the solid domain. This step and step 2 are carried out with increasing depth, or index m . The stopping criterion is when both displacement components (D_z and D_r) are negligibly small.
4. The calculation is then carried out for the next time steps until the final time we desire.

A FORTRAN program is formulated to carry out the calculation. The storage requirement for this program with calculation domain of 60-radial and 60-axial grid points, complete with graphical output subroutine, is 33k words. In the CDC-6500/6600 Dual

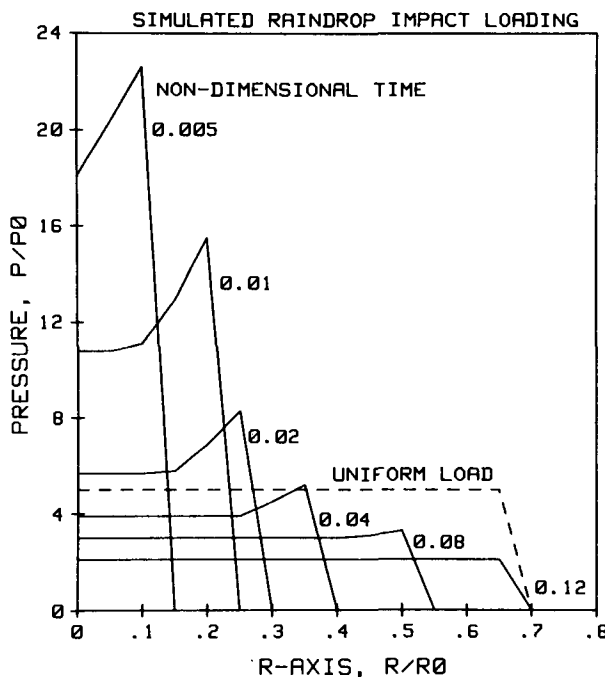


Fig. 2—The simulated load applied on the solid surface at non-dimensional time 0.005, 0.01, 0.02, 0.04, 0.08, and 0.12. The dash-line shows the steady, uniform load of magnitude $5 P_0$.

MACE operating system at Purdue University, a typical run of 240 time steps takes approximately 70 s. The computer time increases with the rigidity of the material that we use in the simulation run. This is simply because the high wave velocities associated with the high Young's modulus increase the range of the influence area within the calculation domain.

In this numerical simulation, we ran two types of loading. They were (i) transient impact loading simulating raindrop impact and (ii) steady uniform loading. The simulated load function is obtained from our previous numerical simulation in the hydrodynamics of the impact (Huang et al., 1982). For the steady uniform loading, we choose a magnitude intermediate among the simulated raindrop impact loading, and set the size of the this uniform load equivalent to the size of the final step of the transient impact load.

The mechanical properties of the ideal elastic material, the Poisson ratio, ν , and the Young's modulus, E , are chosen to represent a typical soil material (p. 567, Winterkorn and Fang, 1975). We set ν equal to 0.35, and use four values of E to represent different degrees of rigidity; they are 1, 2, 4, and 8 MPa ($1 \text{ MPa} = 10^6 \text{ N/m}^2$).

RESULTS AND DISCUSSION

Results shown in this paper are presented in non-dimensional form, with the reference dimensional scales defined as follows: The reference pressure, P_0 ,

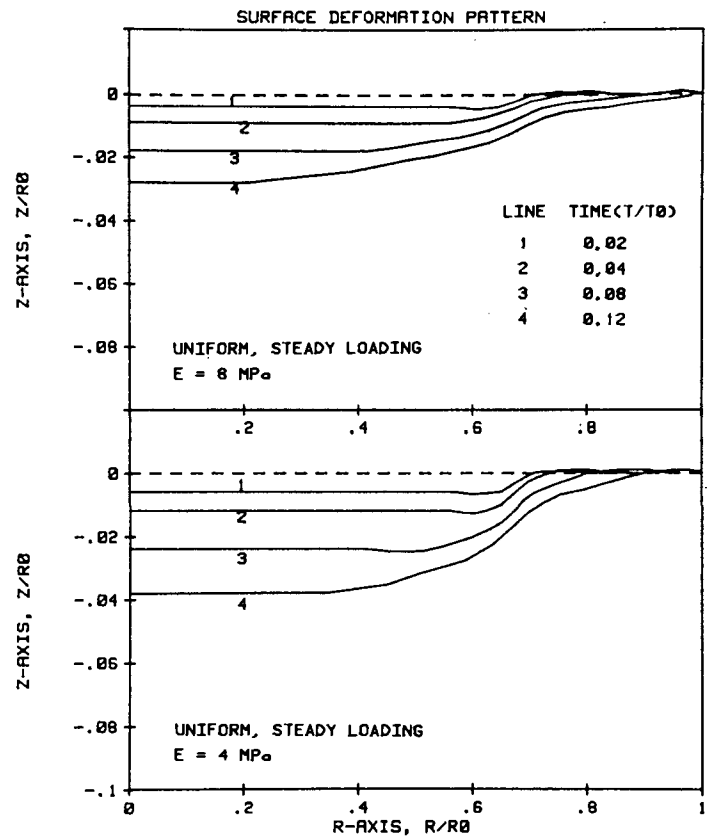


Fig. 3—The surface deformation pattern under steady, uniform load at different time instances after impact. The Young's moduli are 8 and 4 MPa.

is the steady-state stagnation pressure, $0.5\rho_w V_o^2$, where ρ_w is the density of water and V_o is the impact velocity; the reference length is defined as the radius of the drop, R_o ; and the reference time scale, t_o , is defined as R_o/V_o . Thus, for a 4-mm diameter drop falling at 10 m/s, the reference pressure is 50 kPa, the reference time is 200 μ s, and the reference length scale is 2 mm.

We intend to describe our results in the qualitative sense, since we are not actually solving a fully coupled elastic impact problem. The transient impact loading function, $F(r,t)$, was taken from our earlier simulation in rigid impact. Although the actual loading stresses are believed to be less in magnitude for elastic materials compared to the rigid case, the spatial and temporal stress distributions will have similar patterns at the initial stage of the impact (Fyall and King, 1974). Thus the novelty of this study is to show different deformation characteristics. Absolute values are not stressed unless used in the numerical example.

Figure 2 shows the simulated impact loading function, $F(r,t)$, that we have applied on the surface of the elastic material at several selected time instances. For comparison, we also show the uniform load in the same graph by dashline. There are three important points about the raindrop impact loading function that are distinctly different from uniform loading conditions. They are: (i) the magnitudes are very high at the initial time steps, and the load diminishes very quickly; (ii) the distribution is not uniform and the

Table 1—The nondimensional axial displacement at the center of the load under steady, uniform loading condition.

Young's modulus, MPa	Nondimensional time, t/t_o		
	0.04	0.08	0.12
8	0.009	0.018	0.028
4	0.012	0.024	0.037
2	0.017	0.034	0.050
1	0.024	0.047	0.071

Table 2—The nondimensional axial displacement at the center of the load under simulated raindrop impact loading condition.

Young's modulus, MPa	Nondimensional time, t/t_o			
	0.02	0.04	0.08	0.12
8	0.011	0.012	0.012	0.013
4	0.019	0.021	0.022	0.023
2	0.024	0.029	0.035	0.037
1	0.030	0.044	0.057	0.063

maximum occurs at the edge of the contact boundary; and (iii) the area of loading increases with time. Figures 3, 4, 5, and 6 show the time history of the deformation pattern for materials with different moduli of elasticity under different loading conditions. The axial component of the surface displacement at the central axis ($r = 0$) is tabulated in Tables 1 and 2.

From Table 1, we see that the axial displacement changes linearly with time within each elasticity group. The axial displacement vs. time linearity relationship

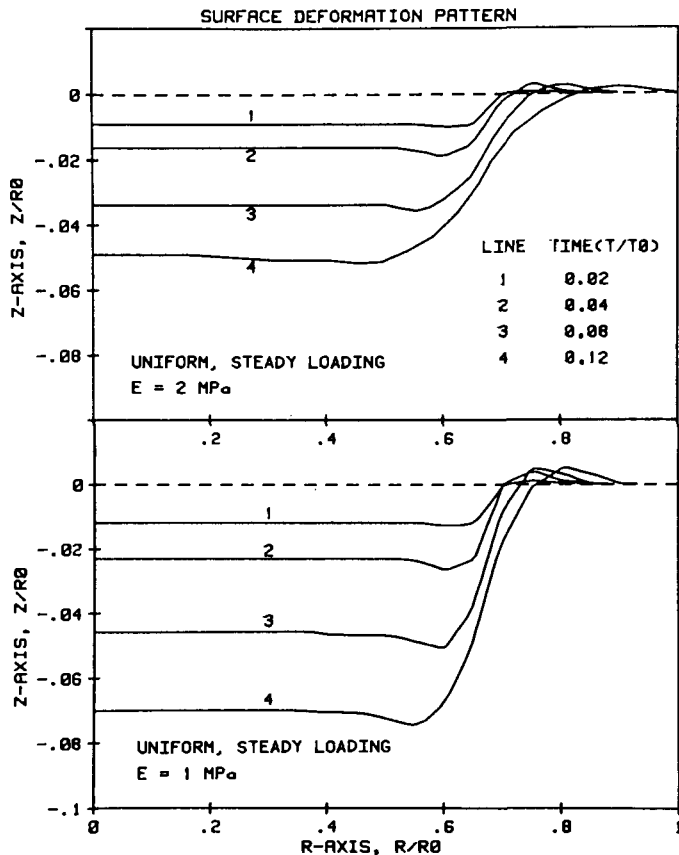


Fig. 4—The surface deformation pattern under steady, uniform load at different time instances after impact. The Young's moduli are 2 and 1 MPa.

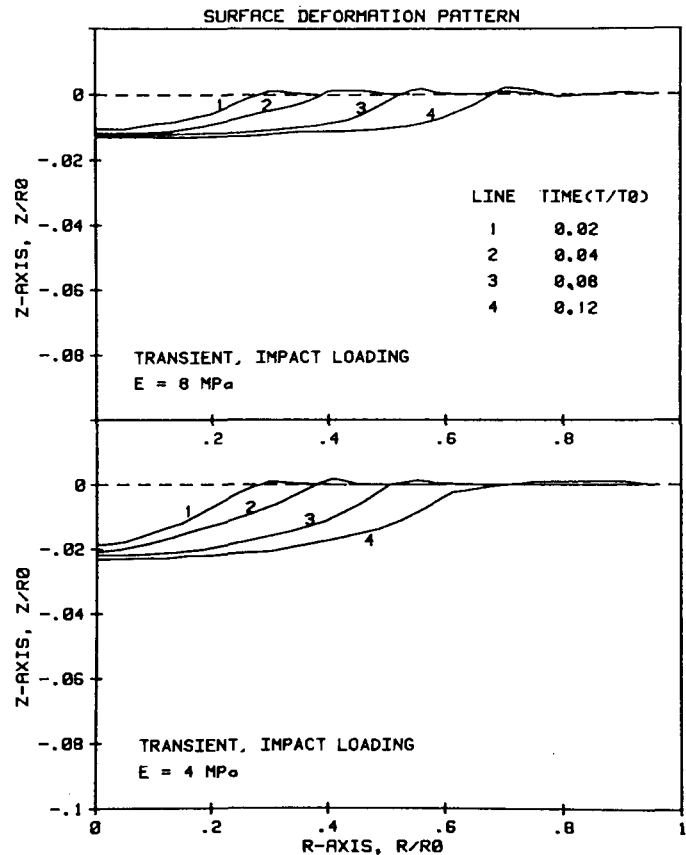


Fig. 5—The surface deformation pattern under simulated raindrop impact load at different time instances after impact. The Young's moduli are 8 and 4 MPa.

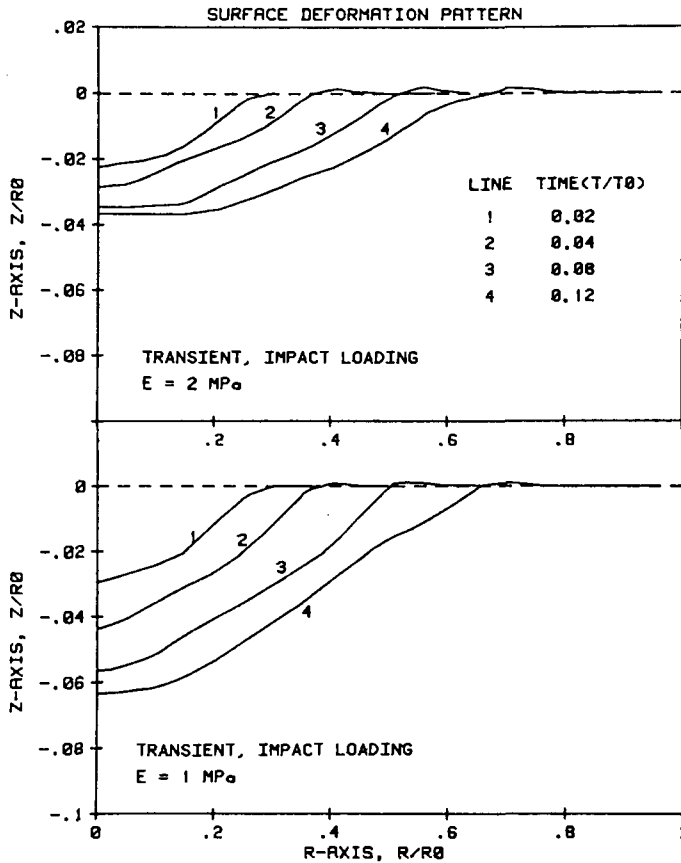


Fig. 6—The surface deformation pattern under simulated raindrop impact load at different time instances after impact. The Young's moduli are 2 and 1 MPa.

is true for areas away from the load/no-load boundary, where uni-axial displacement is dominant. Near the load/no-load boundary, both the axial and radial displacements are important; the linearity no longer holds for the single displacement component. Another point that needs to be made is that we are dealing with an assumed perfect elastic medium with infinite width and depth; however, at time infinity, saying the displacement is infinity is mathematically true, but physically unrealistic. We only intend to study the initial stage of the impact without taking into account the energy dissipation; the time scale is relatively short when compared to the time needed to reach the equilibrium state.

From a plot of surface deformation patterns under uniform load, we see that the boundary effect is more profound in materials with higher Young's moduli (Fig. 3, 4). By the boundary effect, we mean the extent of nonuniformity in displacement as measured from the central axis. In contrast to uniform loading conditions, the displacement patterns under simulated raindrop impact have completely different characteristics (Fig. 5, 6 and Table 2). The more rigid materials acquire most of their surface deformation from the initial high loads; as time progresses and load diminishes, the deformations are observed mainly near the load/no-load boundary. The deformed surface shows a rather uniform depression. For soft materials with low moduli of elasticity, the displacements near the central axis increase continuously without a signifi-

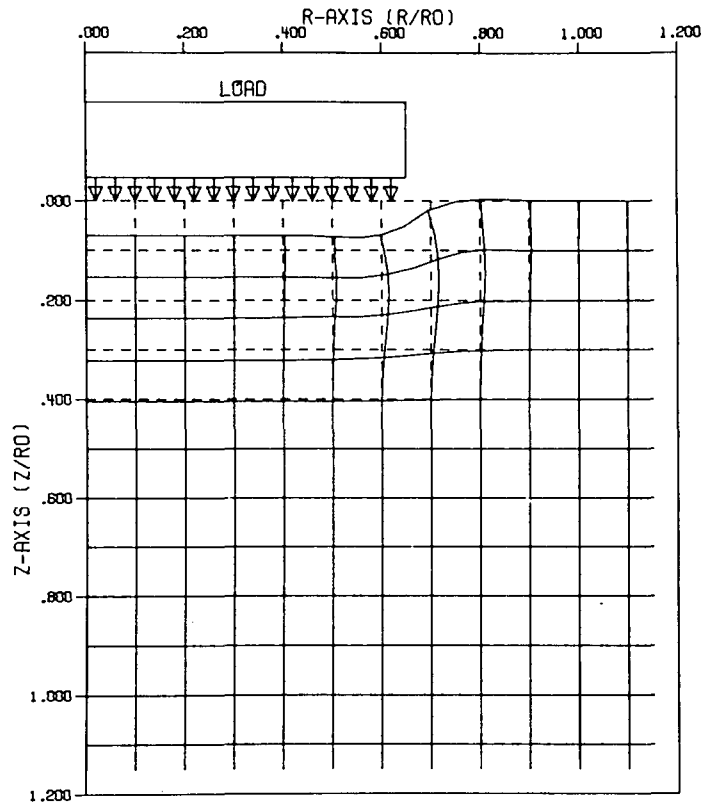


Fig. 7—The deformation pattern within the solid domain under steady, uniform load. The Young's modulus is 1 MPa and the nondimensional time is 0.12.

cant 'slow down' compared to the materials with high rigidity. The cavity not only expands in the radial direction as the loading spreads; it also deepens. The final displaced surface shows a very strong boundary effect.

Figures 7 and 8 are used to demonstrate the displacement within the solid domain for the same material subjected to different loading conditions. Solid lines show the deformed grid system and dashed lines are original grids before loading. In both cases, the axial displacement is dominant near the central axis of the load. The radial displacement of material under uniform loading is observed near the load/no-load boundary. For the case of simulated raindrop impact loading (Fig. 8), the lateral displacements show a cone-shaped distribution inside the solid domain. The lateral zone at which a noticeable lateral displacement is observed is closer to the central axis as the depth increases. This pattern reflects the characteristics of the transient, nonuniform load function, $F(r,t)$, that we have applied on the surface.

Figure 9 shows the displacement distribution for a material with high rigidity. Although the displacement is smaller at the surface for the rigid material, it is carried to a larger depth. This is due to the higher compressional and shear wave velocities associated with the higher modulus of elasticity (Eq. [5] and [6]).

So far, we have shown results of the surface deformation patterns under different loading conditions. Now we want to utilize them to explain the material detachment phenomena under raindrop impact. From an energy standpoint, we can assume that a material

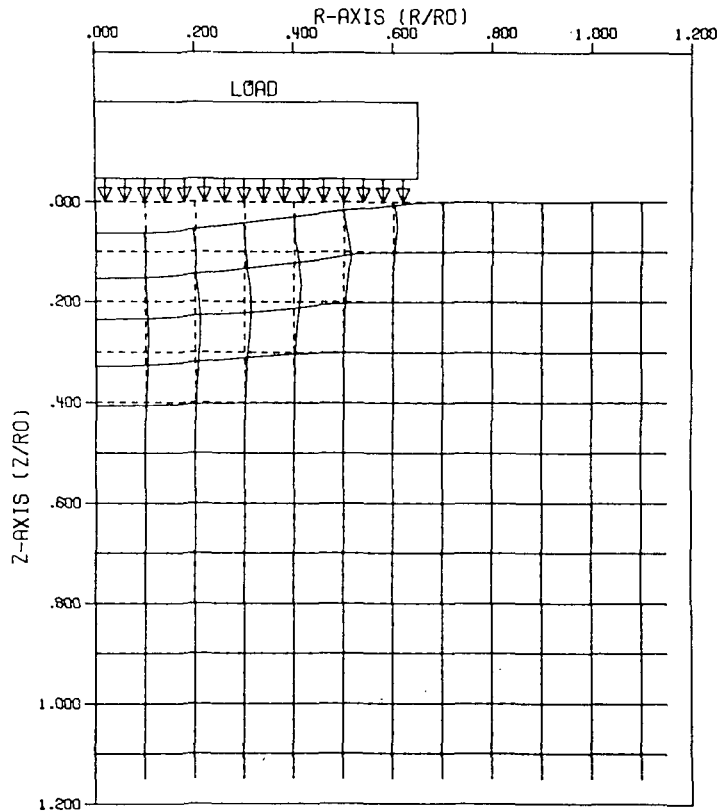


Fig. 8—The deformation pattern within the solid domain under simulated raindrop impact load. The Young's modulus is 1 MPa and the nondimensional time scale is 0.12.

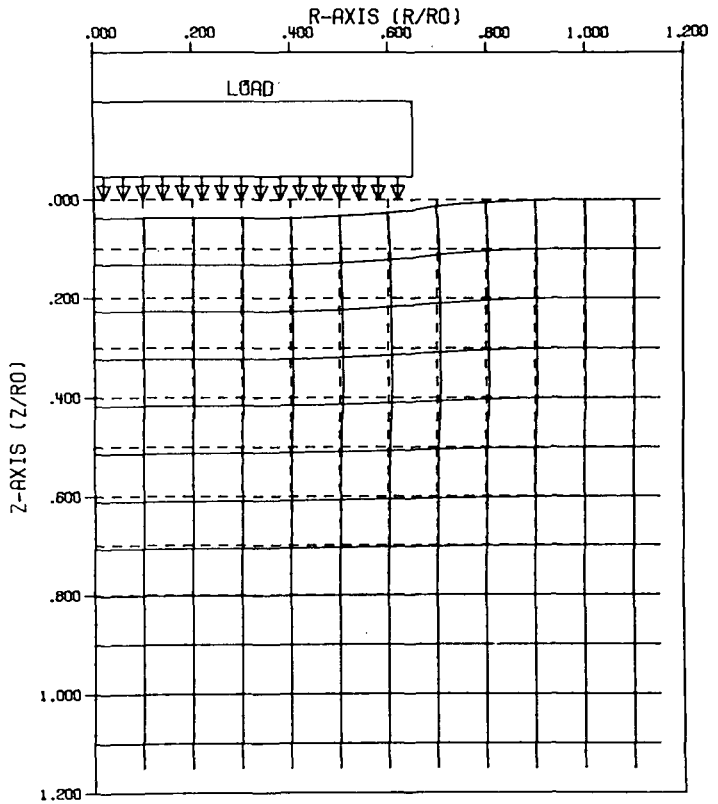


Fig. 9—The deformation pattern within the solid domain under steady, uniform load. The Young's modulus is 4 MPa and the nondimensional time scale is 0.12.

is “destabilized” if we stretch it and is “stabilized” if we compress it. Examining the depression made by the impact loading, we see that the material at the flat bottom of the cavity gains stability due to compression, and material along the rising sides of the cavity is weakened by tensile stretch. At this point, if we impose a high velocity lateral jet stream in the cavity, the sides of the cavity will act as an obstacle in the flow field. The high stagnation pressure on the sides of the cavity will easily erode away the already weakened material. For a more rigid material, it is more likely to have a saucer-shaped depression after impact. This is mentioned by Mihara (1952) in his observations on sand surface after waterdrop impact. For materials with low rigidity, the stabilized area is only confined near the central axis, the inherent low strength on top of the larger areas subjected to the lateral jetting will cause the material to erode more from the cavity. In fact, due to the greater depression and the larger amount of detachment, we only observe a hemispherical dent after impact on soft soils. The granular nature of the soil material further provides more irregularities in the jet stream because a microscopically smooth surface is impossible to obtain.

In conclusion, we have shown the different deformation patterns of materials with different elasticities under steady uniform and simulated raindrop impact loadings. Because of the distinct difference between these two types of loading, the surfaces show different reactions. Under uniform nonrigid loading conditions, the load/no-load boundary effect is more sig-

nificant for high rigidity materials. Under simulated raindrop impact loading, the deformation pattern greatly reflects the nature of the loading; this is especially significant in materials with low modulus of elasticity. The shape of the surface deformation leads us to the conjecture of the mechanism of material detachment. The interaction of the lateral jet stream and the obstacles on its course is believed to be the major mechanism in determining the material detachment. The obstacles can be the sides of the cavity or the irregularities on the granular material itself.

REFERENCES

1. Alterman, Z., and F.C. Karal. 1968. Propagation of elastic waves in layered media by finite difference methods. *Seism. Soc. Am. Bull.* 58:367-398.
2. Fyall, A.A., and R.B. King. (ed.) 1970. *Proc. of Third Int. Conf. on Rain Erosion and Allied Phenomena* (2 vols.) Hampshire, England. 11-13 Aug. 1970. Royal Aircraft Establishment, Farnborough, England.
3. Fyall, A.A., and R.B. King. (ed.) 1974. *Proc. of Fourth Int. Conf. on Rain Erosion and Allied Phenomena* (2 vols.) Meersburg, Germany. 8-10 May 1974. Royal Aircraft Establishment, Farnborough, England.
4. Huang, C., J.M. Bradford, and J.H. Cushman. 1982. A numerical study of raindrop impact phenomena: the rigid case. *Soil Sci. Soc. Am. J.* 46:14-19.
5. Mihara, Y. 1952. *Raindrops and soil erosion*. Nat. Inst. Agric. Sci., Tokyo, Japan. (English translation from Japanese published in July 1951).
6. Richart, E. Jr., J.R. Hall, Jr., and R.D. Woods. 1970. *Vibrations of soils and foundations*. Prentice Hall Inc., Englewood Cliffs, N.J.
7. Winterkorn, H.F., and H. Fang. (ed.) 1975. *Foundation engineering handbook*. Van Nostrand Reinhold Co., New York.